

# Corrosion Behavior and Surface Modification of Mg-Zn Implant Alloys

I.M. Ghayad , M.A. Maamoun, W.A. Metwally, Z.M. El-Baradie, and A.N. Abdel-Azim

(Submitted July 2, 2015; in revised form March 26, 2016; published online August 17, 2016)

**In this study, Mg-Zn alloys (1-4 wt.% Zn) were fabricated with high-purity raw materials using a clean melting process (fluxless method) and a protective atmosphere of CO<sub>2</sub> + 0.4 SF<sub>6</sub>. The as-cast microstructures of the investigated alloys were characterized by optical and scanning electron microscopes, EDS and XRD. Corrosion properties of the prepared alloys were examined in simulated body fluid by electrochemical techniques and immersion test (hydrogen evolution method). Surface modification of the prepared alloys was performed using micro-arc oxidation (MAO) treatment and hydroxyapatite (HA) coating. Microstructure observation revealed that Zn was completely dissolved in the α-Mg matrix up to 2 wt.%. Higher Zn content led to a reduction in the grain size and the development of a second phase (MgZn<sub>2</sub>). Corrosion testing results revealed that Mg-1,2,3 wt.% Zn have almost the same degradation rate, whereas Mg-4Zn has the highest degradation rate. HA coating on MAO-treated magnesium alloys formed a dense and compact layer on the alloy surface, which had largely improved surface properties and enhanced corrosion resistance of the prepared alloys.**

**Keywords** biodegradable, corrosion, implants, Mg alloys, surface modification

## 1. Introduction

There has been an increasing interest in magnesium alloys as a biodegradable metal implants in orthopedic surgery, because of its biocompatibility, biodegradability and similar mechanical properties to natural bones (Ref 1).

The major limitation of magnesium is its low corrosion resistance, which could result in a reduction in the mechanical integrity of the implant before sufficiently healing of bones or tissues (Ref 2). It also leads to a rapid production of hydrogen gas and the formation of gas bubbles, which can accumulate around the implant delaying healing of the tissue (Ref 3). Localized formation of hydrogen gas results in a pH increase around the implant, which severely affects the pH-dependent physiological process in the vicinity of the implant (Ref 1, 4). Therefore, a significant, uncontrolled, local change in Mg concentration due to implant degradation must be managed through proper engineering design. Controlling the Mg degradation rate could be attained by microstructure modification, additions of alloying elements and surface treatment (Ref 5-9).

Studies showed that purification of Mg considerably reduces the corrosion rate; however, due to the low yield strength of pure Mg, its application in orthopedics and other load-bearing applications is limited (Ref 1).

Alloying elements added to increase the strength of pure Mg should be carefully selected to maintain the Mg's biocompatibility and to reduce toxicity (Ref 10, 11). Zn is one of the

essential elements in the human body and could be safely used for biomaterial applications. Zn acts as grain-refining element and improves corrosion resistance and mechanical properties. It also helps to overcome the harmful effect of iron and nickel impurities that might be exist in Mg alloys. Mg-1Zn produced less hydrogen gas than many other binary Mg alloys in simulated body fluid. Zn ion concentration up to 60 ppm did not cause cell toxicity (Ref 12, 13).

Micro-arc oxidation (MAO) is a chemical conversion coating of the substrate metal into its oxide. Unlike anodizing, MAO employs higher potentials, so that discharges occur generating plasma which modifies the oxide layer structure. MAO can be used to grow thick, largely crystalline, oxide coatings on metals such as aluminum, magnesium and titanium. MAO coatings can offer protection against wear, aqueous and high-temperature corrosion because they can present high hardness and a continuous barrier. It grows both inwards and outwards from the original metal surface, and it has excellent adhesion to the substrate metal (Ref 14-17).

MAO could fabricate porous ceramic coating with high adhesion to substrate, which can be used as the intermediate layer for depositing hydroxyapatite (HA). When HA is deposited in the pores, it generates pinning force and enhances the corrosion resistance of the porous layer. Thus, fabricating HA coating on the MAO layer may be a promising way to improve the biocompatibility and corrosion resistance of magnesium alloys. The corrosion-resistant film formed on a magnesium implant should also be wear resistant so that the film will not be damaged by scratching during implanting (Ref 1, 18).

Based on the above considerations, Zn was selected as an alloying element to develop cast Mg implant alloys with varying Zn content (1-4 wt.%) using fluxless method. The effect of zinc content on the microstructure and corrosion behavior of the Mg-Zn alloys was thoroughly investigated. The performance of the prepared alloys using MAO/HA coating was also studied.

I.M. Ghayad, M.A. Maamoun, W.A. Metwally, Z.M. El-Baradie, and A.N. Abdel-Azim, Central Metallurgical Research and Development Institute (CMRDI), P.O. Box 87, Helwan, Cairo, Egypt. Contact e-mail: ighayad@yahoo.com.

## 2. Experimental Procedure

### 2.1 Materials and Preparation

Magnesium-zinc alloys were prepared using pure magnesium (99.9%) and pure zinc (99.99%) ingots as a starting material. Melting and alloying operations were carried out at 750 °C in mild steel crucible using resistance electric furnace under the protection of a gas mixture of CO<sub>2</sub> + 0.4% SF<sub>6</sub>. Zn was added in the range 1-4 wt.%. The melt was mechanically stirred and kept after stirring for 10 min at 750 °C to ensure complete dissolution of the alloying elements in the melt. The molten metal was skimmed periodically. Finally, the melt was cast into cast iron mold preheated to 250 °C. The chemical compositions of the prepared Mg-Zn alloys were determined using Niton XL3t XRF mobile analyzer and are presented in Table 1.

### 2.2 Microstructure Characterization

Samples were prepared using metallographic techniques adapted for magnesium alloys. Successive grinding up to 2000 SiC grit paper was carried out. The samples were polished using 0.25- $\mu$ m diamond paste and immersed in the diamond coolant solution for a few minutes to avoid oxidation. The samples were then washed with distilled water followed by ethyl alcohol and dried in warm flowing air. For microstructure examinations by optical and scanning electron microscopes, the as-cast samples were electrolytically polished and etched in a solution containing 625 mL ethanol (95%) and 375 mL phosphoric acid (85%) under cell volt of  $\sim$ 2 V using steel plate as cathode. A Zeiss Axiovert optical microscope was used for microstructure investigation. Scanning electron microscope (SEM, JEOL, JSM 5410, Japan) equipped with energy-dispersive spectroscopy (EDS) unit was used for surface morphology investigation.

### 2.3 Corrosion Tests

#### 2.3.1 Immersion Tests (Hydrogen Evolution Method).

Simulated body fluid (SBF) was used as the test solution for all corrosion tests (Table 2). Tests were carried out at room temperature and pH 7.9. Corrosion rates were calculated using hydrogen gas evolution method. It is well established that hydrogen evolution method is the best approaches in this respect, since it has been demonstrated theoretically and experimentally that the amount of hydrogen collected is equal to the amount of magnesium dissolved. An ideal device, easy

and simple to operate, was set up, as shown in Fig. 1. Disk specimens of 1.2 cm diameter were immersed in a 500- to 600-mL beaker containing 450 mL of the test solution, prepared using distilled water and analytical grade chemicals. A funnel was placed over the specimen to ensure the collection of all the hydrogen evolved from the specimen surface as well as from any undermined metal particles at the bottom of the beaker. A 50-mL buret initially full of test solution was mounted over the funnel. The beakers were tightly covered to avoid solution evaporation. The volume of hydrogen gas evolved was easily measured by reading the position of the test solution levels in the buret. Test duration was 170 h and monitored every 24 h. The measured hydrogen volume can be easily converted into g moles using the ideal gas law. Simply assuming that the number of moles of the evolved hydrogen is equal to the number of moles of the dissolved magnesium, weight loss or degradation rate of the specimen was then calculated (Ref 19, 20).

#### 2.3.2 Electrochemical Tests (Potentiodynamic Polarization Test).

Electrochemical tests were carried out in a three-electrode cell using a platinum electrode as the counter electrode, Ag/AgCl electrode as the reference electrode and the tested specimen as the working electrode. The working

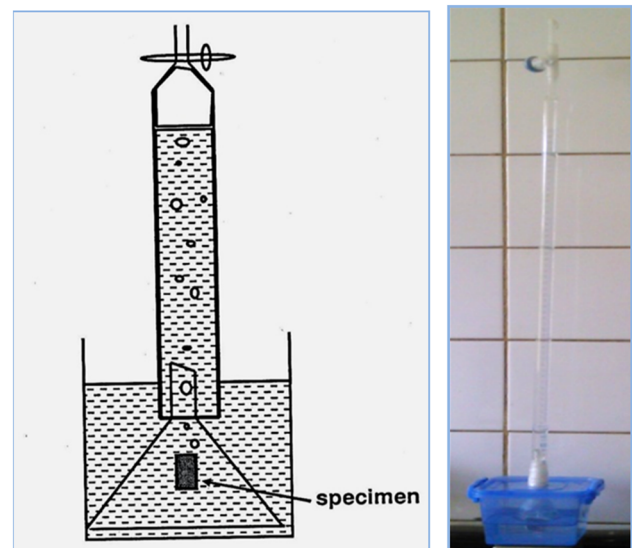


Fig. 1 Schematic and implemented device for hydrogen evolution test

Table 1 Chemical compositions (wt.%) of the as-cast Mg alloys

| Alloy  | Symbol | Zn   | Al   | Si  | Fe   | Mg   |
|--------|--------|------|------|-----|------|------|
| Mg-1Zn | Z1     | 1.2  | <0.3 | 0.3 | 0.00 | Bal. |
| Mg-2Zn | Z2     | 2.1  | <0.3 | 0.3 | 0.01 | Bal. |
| Mg-3Zn | Z3     | 3.16 | <0.3 | 0.3 | 0.01 | Bal. |
| Mg-4Zn | Z4     | 4.11 | <0.3 | 0.3 | 0.03 | Bal. |

Table 2 Chemical composition of SBF

| Chemicals        | NaCl | KCl | CaCl <sub>2</sub> | NaHCO <sub>3</sub> | C <sub>6</sub> H <sub>6</sub> O <sub>6</sub> | MgSO <sub>4</sub> ·7H <sub>2</sub> O | KH <sub>2</sub> PO <sub>4</sub> ·H <sub>2</sub> O | Na <sub>2</sub> HPO <sub>4</sub> ·7H <sub>2</sub> O |
|------------------|------|-----|-------------------|--------------------|--|--------------------------------------|---|---|
| Composition, g/L | 8.8  | 0.4 | 0.14              | 0.35               | 1  | 0.2                                  | 0.1   | 0.06  |



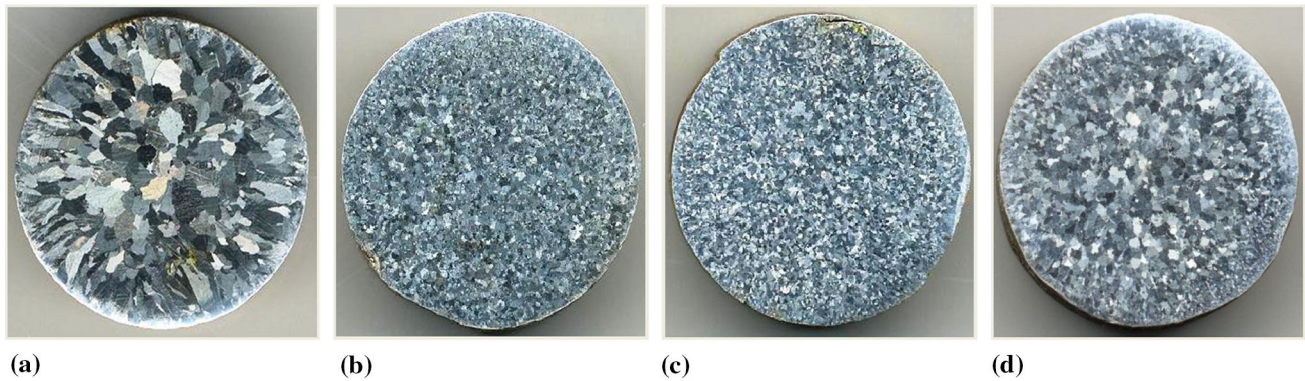


**Fig. 2** Macrostructures of as-cast Mg-Zn alloys samples having a diameter of 1.4 cm; (a) Z1, (b) Z2, (c) Z3, (d) Z4

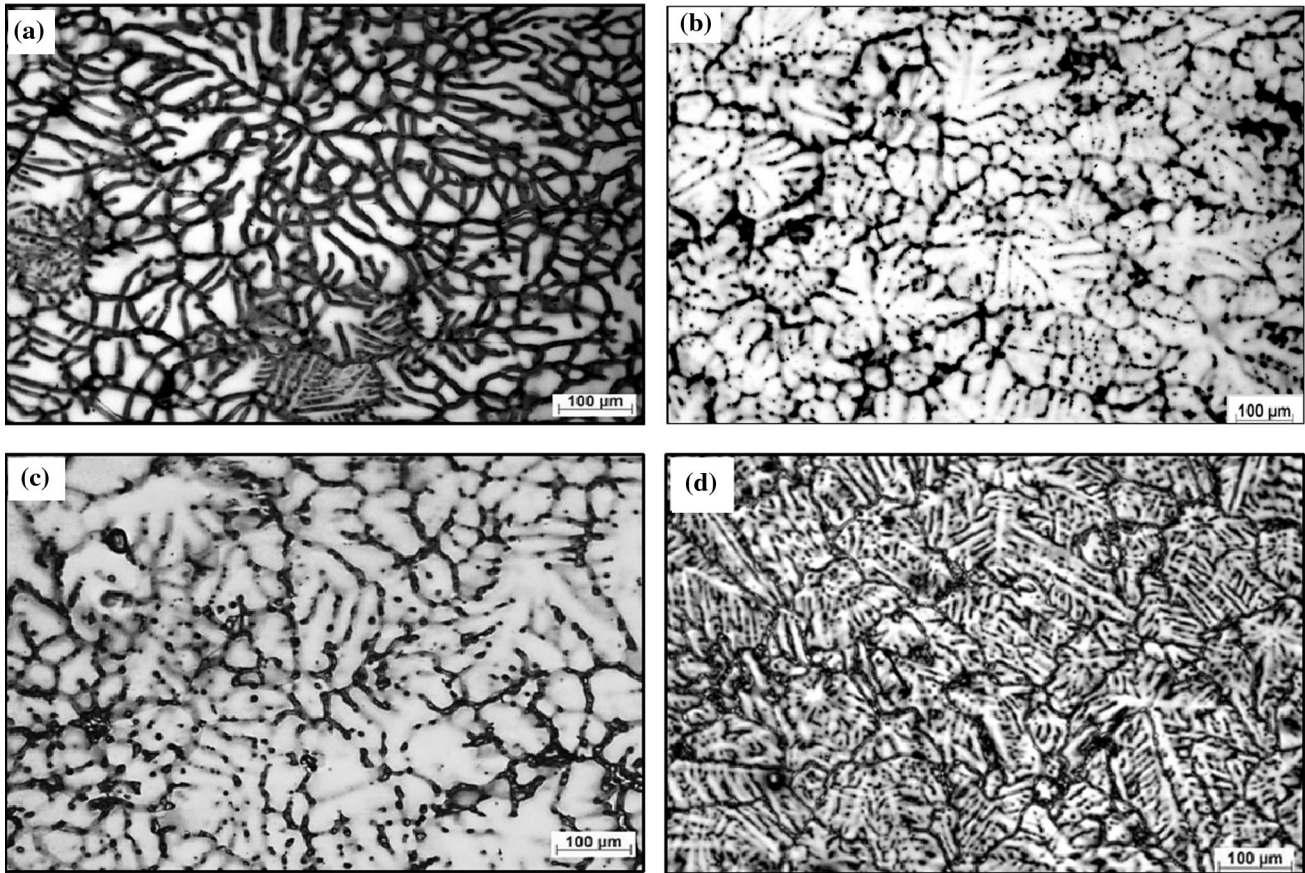


**Fig. 3** Optical microstructures of as-cast Mg-Zn alloys (a) Z1, (b) Z2, (c) Z3, and (d) Z4

electrode (tested specimen) was immersed in the SBF testing solution for half an hour at room temperature before carrying out the test in order to attain a steady-state corrosion potential ( $E_{\text{corr}}$ ). Tests were performed using a potentiostat (Auto Lab PG Stat 30 Corrosion Measurement System). Potentiodynamic scan was carried out starting at  $-0.3$  up to  $1.0$  V with respect to free corrosion potential  $E_{\text{corr}}$  at a scan rate of  $1$  mV/s.

## 2.4 Surface Coating Investigation

**2.4.1 Micro-arc Oxidation Treatment.** Ceramic magnesium oxide coating was prepared on the magnesium alloys using an alternating current ( $10$  A,  $100$  V and  $50$  Hz) micro-arc

discharge in a specific electrolyte composed of  $15$  g/L sodium silicate and  $5$  g/L potassium hydroxide under temperature controlled below  $50$  °C for about  $2$  min. Disks of  $1.5$  mm thickness machined from the magnesium alloy bar were used as the substrate material. MAO process was carried out using a high AC power supply unit, a stainless-steel counter electrode and a cooling system. Prior to MAO process, the specimens were successively ground with  $600,800$  and  $1200$  grit paper, followed by alumina polish ( $0.25$  μm), then rinsed with distilled water, degreased with ethyl alcohol and dried in a cool air stream. During the early stages of the MAO treatment and on increasing voltage, the plasma appears as sparks moving across the specimen surface allowing the oxidation process to

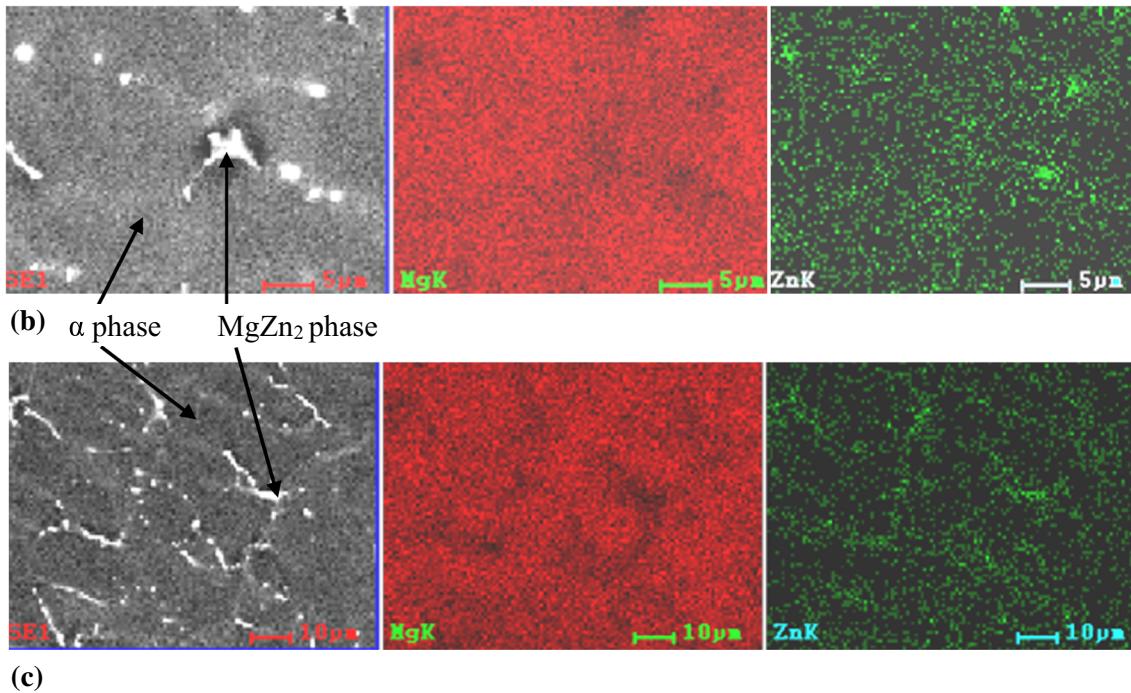
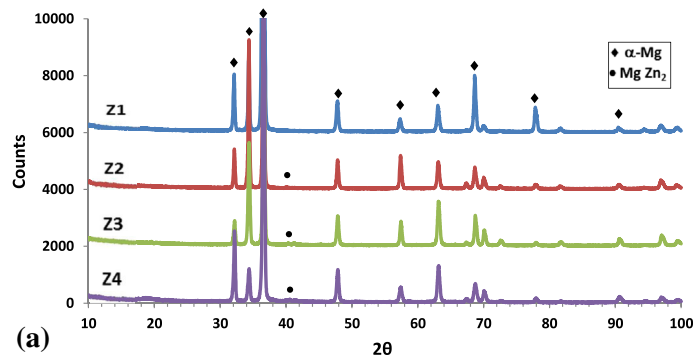


**Fig. 4** (a) XRD of as-cast Mg-Zn alloys, (b) elemental distribution map of Z2, (c) elemental distribution map of Z4

go on. The sparks become micro-arc before changing into arcs. Through this process, fast formation of thick, dense and hard ceramic layer was observed (Ref 14-17).

The adhesion properties of the MAO coating were performed using the adhesion tape test to assess the adhesion between the micro-arc oxidation layer and magnesium alloys substrate by applying and removing pressure-sensitive tape over “X” cuts made in the film. The test was carried out according to ASTM D3359 standard test methods for measuring adhesion by tape test.

#### 2.4.2 Preparation of Hydroxyapatite (HA) Coating.

The MAO-treated magnesium alloy was introduced into HA coating solution. The HA solution is composed of calcium nitrate (8 g/L) and sodium dihydrogen phosphate (4 g/L). The samples were immersed in the HA coating solution for 30 min under microwave radiation, followed by rinsing with distilled water and then drying at 350 °C for 3 h.

### 2.5 Surface Characterization

Bruker AXS-D8 x-ray diffractometer with  $\text{CuK}\alpha$  radiation source with step scan rate of  $0.02^\circ$  was used for the

identification of the constituent phases in the as-cast Mg-Zn alloys and the determination of phases volume fractions. It is also used for the determination of phase composition of MAO and HA coatings. The morphology and composition of uncoated and coated samples were observed under scanning electron microscope (SEM, JEOL, JSM 5410, Japan) equipped with energy-dispersive spectroscopy (EDS) unit.

## 3. Results and Discussion

### 3.1 Microstructure Investigation of Mg-Zn Alloys

Figure 2(a)-(d) shows macrostructures of the as-cast Mg-Zn alloys. The increase in Zn content has resulted in grain refinement. The maximum reduction in grain size is observed for Z2 and Z3 alloys. Average grain sizes of 0.68, 0.319, 0.346 and 0.399  $\mu\text{m}$  are observed for Z1, Z2, Z3 and Z4, respectively. Figure 3(a)-(d) represents typical microstructures of the as-cast Mg-Zn alloys. Dendritic and interdendritic structures are observed. XRD analysis was used to identify



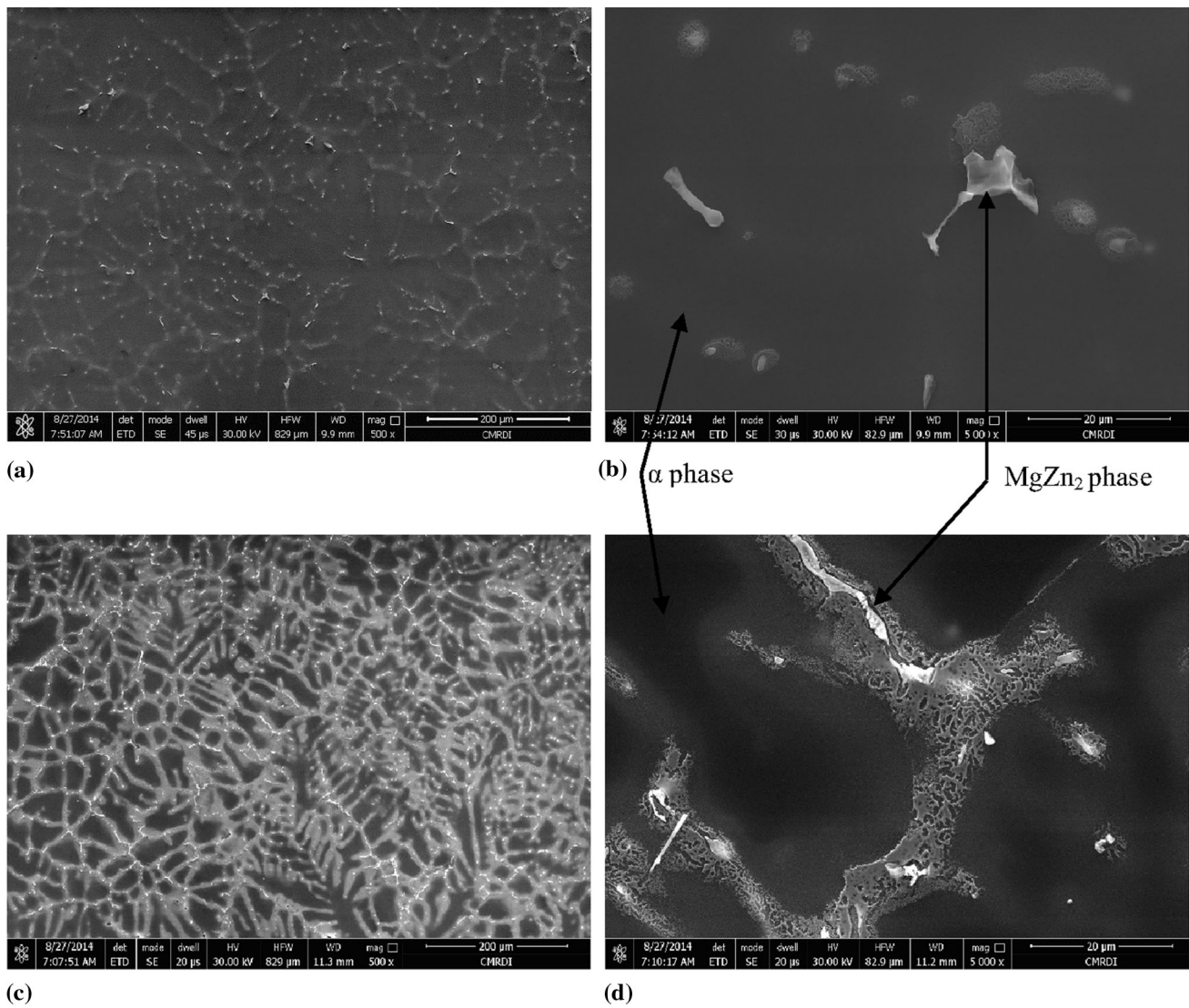


Fig. 5 SEM micrographs of as-cast Mg-Zn alloys; (a,b) Z2 and (c, d) Z4

intermetallic phases in the Mg-Zn alloys (Fig. 4a). There are only diffraction peaks of  $\alpha$ -Mg phase in Z1 alloy (1 wt.% Zn). As Zn content increases, diffraction peaks of  $\text{MgZn}_2$  phase's pattern are detected. At 2 wt.% Zn (alloy Z2), Zn was dissolved in Mg matrix as solid solution and small amount of  $\text{MgZn}_2$  second phase precipitated from matrix. At higher Zn content (alloys Z3 and Z4), the microstructure obviously changed and more second phase ( $\text{MgZn}_2$ ) was precipitated. The volume fractions of  $\text{MgZn}_2$  phase are determined from XRD charts using the instrument software. Volume fractions of 2.6, 4 and 4.6% are observed for Z2, Z3 and Z4, respectively. The crystal structure of pure magnesium is hexagonal close packed (HCP). The lattice parameters of pure magnesium are  $a = 0.32092$  nm and  $c = 0.52105$  nm; thus, the  $c/a$  ratio is 1.6236. This actual value of  $c/a$  is very close to that of the ideal HCP crystal structure (1.633) (Ref 21). The  $\text{MgZn}_2$  Laves phase has a hexagonal structure (space group  $P63/mmc$ , with  $a = 0.5221$  nm and  $c = 0.8567$  nm) (Ref 22). The refinement efficiency of zinc was previously determined (Ref 23, 24) by its growth restriction factor (GRF)  $Q$ , which is a measure of the

segregating power of an element during solidification and is expressed by the following equation:

$$\text{Growth restriction factor} = \sum_i m_i C_{0,i} (k_i - 1)$$

where  $m_i$  is the slope of the liquidus line (assumed to be straight),  $k_i$  is the distribution coefficient and  $C_{0,i}$  is the initial concentration of element  $i$ . The GRF values of Zn are 5.31. Zn plays an important role in controlling the growth of the nucleated grains and in subsequent nucleation. Zn segregates strongly in the melt and causes intense constitutional super cooling in a diffusion layer ahead of the advancing solid/liq-uid interface, consequently promoting nucleation and restricting grain growth.

The elemental distribution map of Z2 and Z4 (Fig. 4b, c) proves segregation of Zn element at grain boundaries. SEM micrographs (Fig. 5) show that the second phase ( $\text{MgZn}_2$ ) has strip, rod-like and elliptical shapes. The amounts of this phase are increased by increasing Zn content (Fig. 5b, d). Meanwhile, continuous and discontinuous lamellar eutectic structures were observed in the microstructure. The thickness of the lamellar

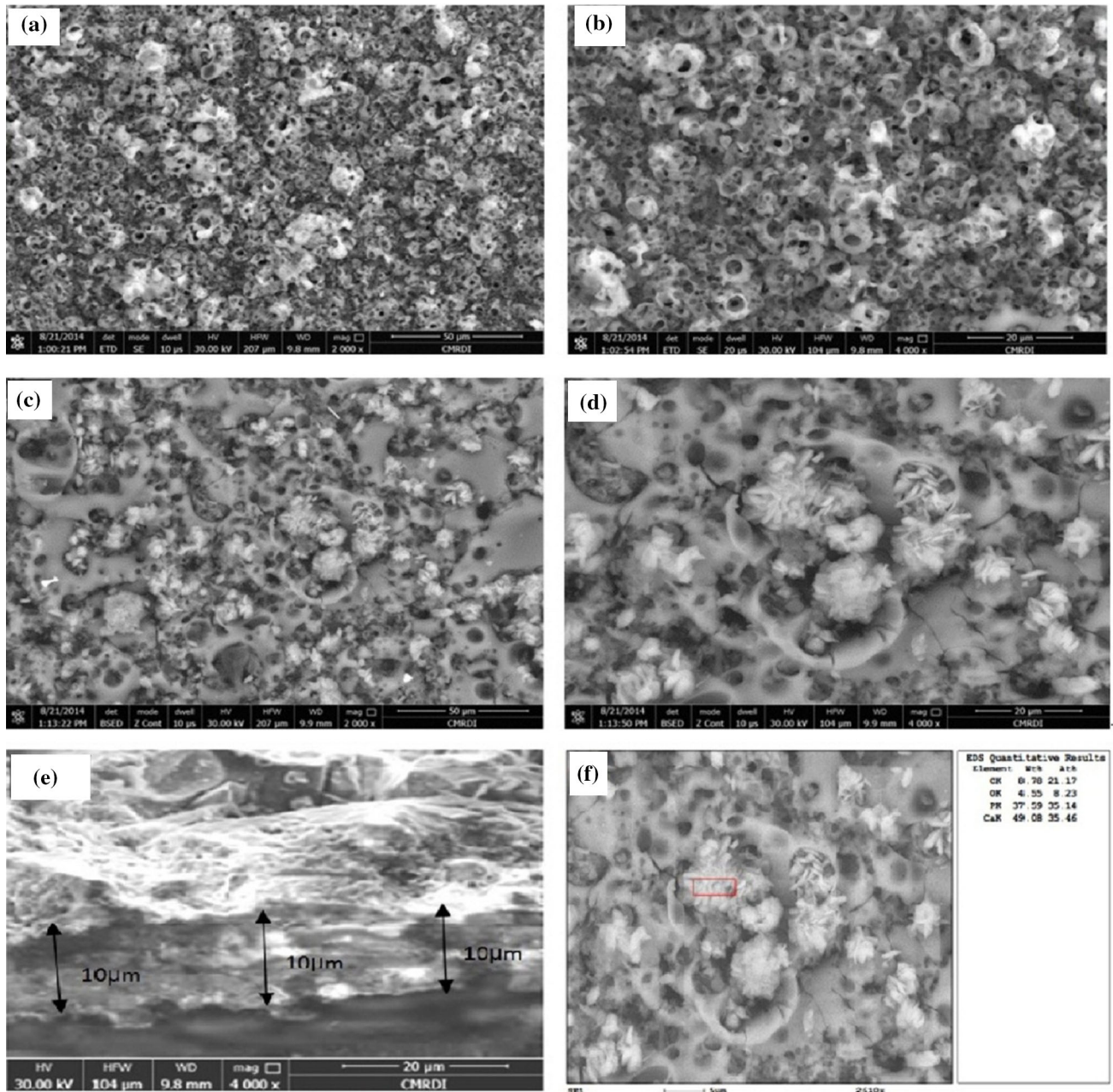


**Fig. 6** SEM morphology of MAO and MAO/HA-coated Z1 alloy; (a, b) MAO, (c, d) MAO/HA, (e) cross-sectional MAO/HA coating. Image (f) represents the EDS analysis of HA

structure appears to have increased significantly with increasing Zn content. These eutectic structures are coarse and mostly distributed in the grain boundaries rather than in the areas of interdendrite (Fig. 5d).

### 3.2 Micro-arc Oxidation/Hydroxyapatite Surface Coating Morphology

Surface morphology of the MAO-treated magnesium alloys is shown in Fig. 6(a) and (b). A porous ceramic oxide film was formed throughout the surface with a layer thickness of 10 µm (Fig. 6e). The MAO coating is composed of a dense inner layer and a porous outer layer. Round pores of 2-5 µm diameters are shown in the porous outer layer. Previous studies (Ref 25-27) showed that the micropores were formed by molten oxide and

gas bubbles thrown out of micro-arc discharge channels, and the cracks resulted from the thermal stress due to the rapid solidification of the molten oxide in a relatively cold electrolyte.

The cross-hatch tape test was used to assess the adhesion between the micro-arc oxidation layer and magnesium alloy substrate. Adhesion is assessed on a zero to five as follows:

- 5A: no removal or peeling.
- 4A: Trace peeling or removal along incisions.
- 3A: Jagged removal along incisions up to 1.6 mm on either side.
- 2A: Jagged removal along incisions up to 3.2 mm on either side.



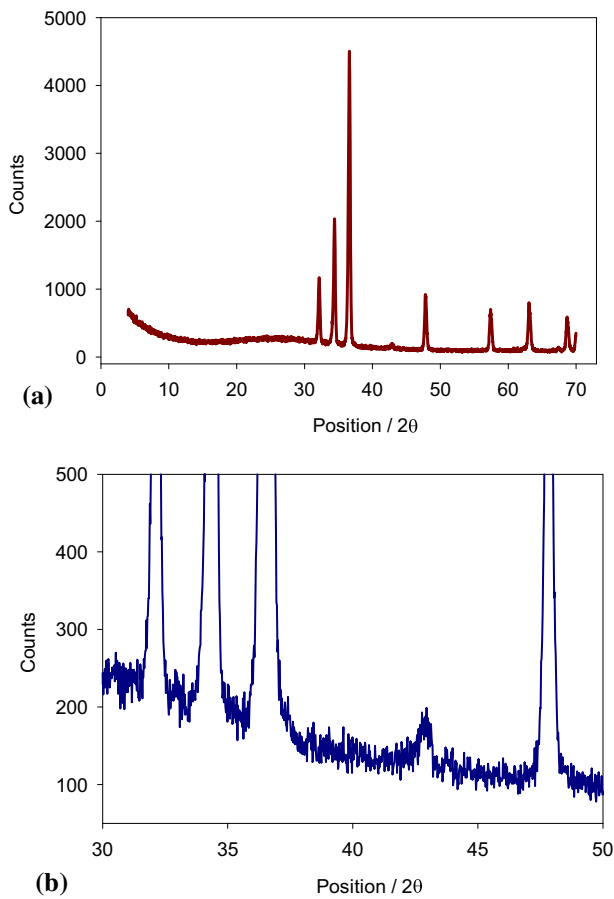
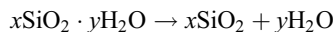
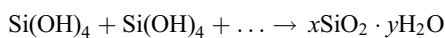
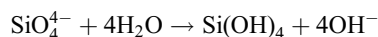


**Fig. 7** (a) XRD pattern of MAO coating on Z1 alloy; (b) is a magnified part of (a) that shows the MgO peak.

1A: Removal from most of the area of the X under the tape.  
 0A: Removal beyond the area of the X.

All micro-arc oxide layers adhere well with the magnesium alloy substrate layer without peeling off. Z1, Z2, Z3 and Z4 MAO-coated samples are rated 5 (no removal or peeling) on the adhesion scale. The bipolar current mode used in this study is expected to improve the coating quality compared with the unipolar current mode, in terms of surface morphology and cross-sectional microstructure.

The XRD pattern (Fig. 7) has shown that the MAO ceramic coating is mainly composed of MgO phase and Mg<sub>2</sub>SiO<sub>4</sub>. In aqueous solution of MAO electrolyte, the sodium silicate is easily hydrolyzed to Si(OH)<sub>4</sub>. Under condition of high temperature resulting from discharge during the micro-arc oxidation process, Si(OH)<sub>4</sub> is dehydrated to SiO<sub>2</sub> through the following reaction (Ref 28):



Some SiO<sub>2</sub> and MgO transform into Mg<sub>2</sub>SiO<sub>4</sub>. Finally, a mixture of MgO and Mg<sub>2</sub>SiO<sub>4</sub> coexists in the XRD pattern.

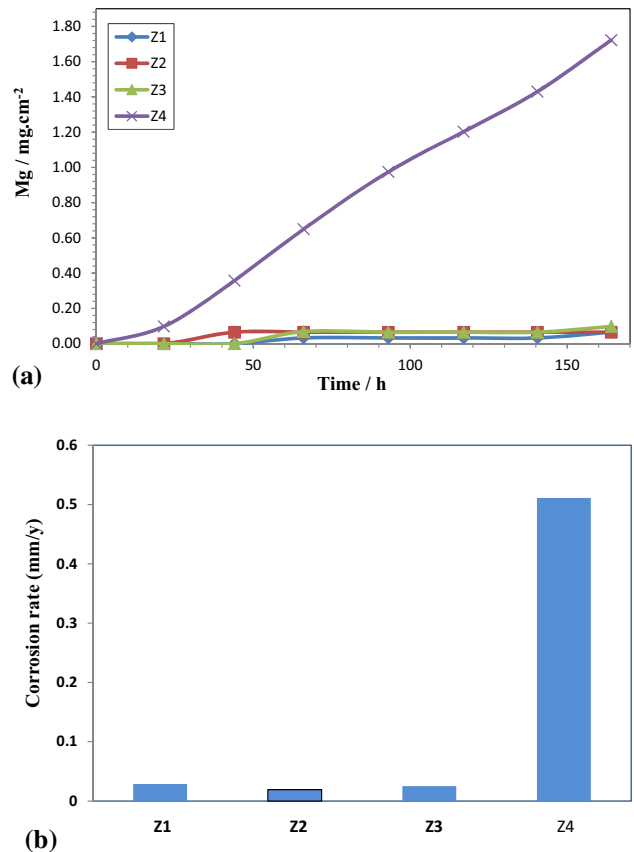


**Fig. 8** Degradation rates (a) and histogram of corrosion rates (b) of the as-cast Mg-Zn alloys calculated after 7 days immersion in SBF solution



After HA treatment (Fig. 6c, d), the large pores on the MAO-treated alloys became smaller (2 μm) and some of them were sealed due to the formation of fine dendritic structure of HA. After MAO/HA treatment, coating is not dense enough and many pores were found on the surface. The pores could be beneficial for the infiltration of new bone tissues into the implants and accelerating the healing process (Ref 29, 30). The fine dendritic structure of the HA coating was helpful for bone growth.

The formation of HA observed in Fig. 5(c) and (d) was confirmed by EDS composition analysis, as shown in Fig. 5f. Ca and P were detected in the porous MAO layer. Carbon element (C) was detected in the HA coating possibly caused by the dissolution of CO<sub>2</sub> from surrounding atmosphere. CO<sub>3</sub><sup>2-</sup> might substitute the PO<sub>4</sub><sup>3-</sup> in the apatite, producing a coating that has a similar composition to the biological apatite from natural bone mineral, which is beneficial to the biocompatibility (Ref 31).

### 3.3 Corrosion Investigation of Mg-Zn Alloys

**3.3.1 Hydrogen Evolution Test.** Based on the measured hydrogen gas produced, the degradation rates of the as-cast Mg-Zn alloys are calculated and presented in Fig. 8(a). Duplicate samples of each alloy were tested. The difference in degradation rates shown by duplicates was found to be within experimental error. Corrosion rates in mm/y after 170-h

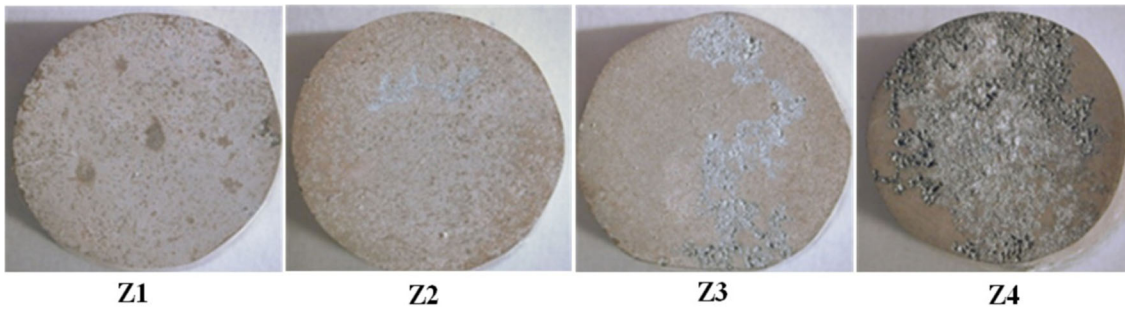


Fig. 9 Macrographs of the as-cast Mg-Zn alloys samples (1.13 cm<sup>2</sup>) after 7 days immersion test

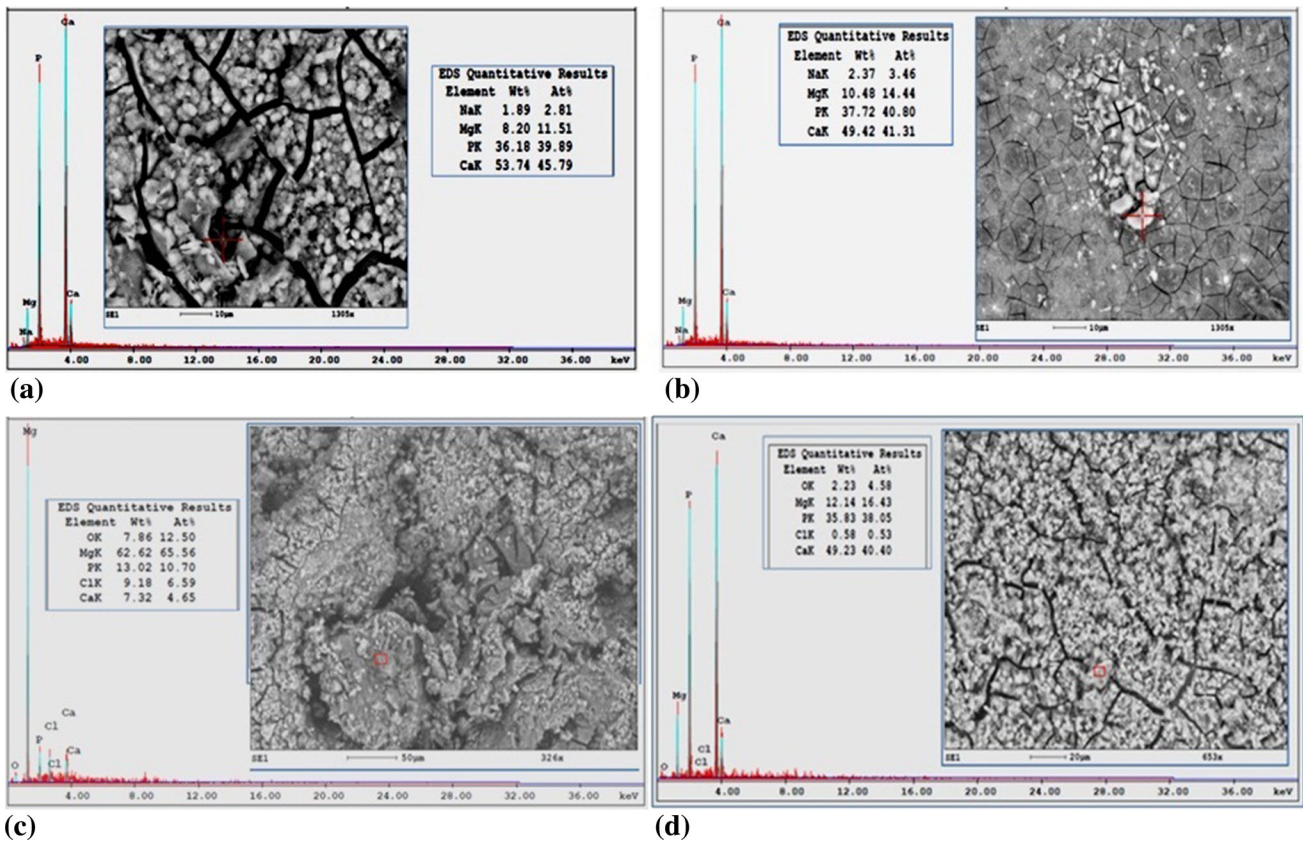


Fig. 10 SEM and EDS of Z1 and Z4 alloys after 7 days immersion test; (a) EDS on Z1 alloy surface, (b) EDS on Z1 deposits, (c) EDS on Z4 alloy surface, (d) EDS on Z4 deposits

immersion are presented in histogram, as shown in Fig. 8(b). Mg-Zn alloys Z1, Z2, Z3 have shown very low corrosion rates ( $<0.03$  mm/year) through the total immersion period, whereas Z4 has shown an almost linear increase up to the 170-h immersion. This was mainly attributed to precipitation of second cathodic phases and absence of continuous protective film as formed on Mg-1,2,3 wt.% Zn alloys (Ref 32).

Surface morphologies of samples of Mg-Zn alloys soaked in SBF for 170 h are shown in Fig. 9. For these alloys, pitting corrosion is almost insignificant on Z1 and Z2. It started to show as shallow laterally spread pits on Z3, whereas Z4 is the most severely attacked sample in this group. The presence of precipitates or the cathodic phases in Z3, Z4 led to selective

attack of the matrix around these phases and its peeling off the surface leaving pits behind. These pits grow in size and agglomerate into irregular array from which dramatic evolution of hydrogen takes place (Ref 33). Z1 and Z4 samples were examined under SEM equipped with EDS (Fig. 10). Z1 sample has shown almost intact surface with few shallow cracks due to hydrogen evolution at low rate; peaks of P and Ca were detected indicating the formation of protective calcium phosphate layer (Fig. 10a, b). On the other hand, Z4 sample showed more pronounced pitting attack spreading on the surface, where peaks of Mg rather than Ca or P were detected (Fig. 10c, d). Relatively small dispersed areas were found to have Ca and P peaks, indicating that the surface of the corroded specimen is



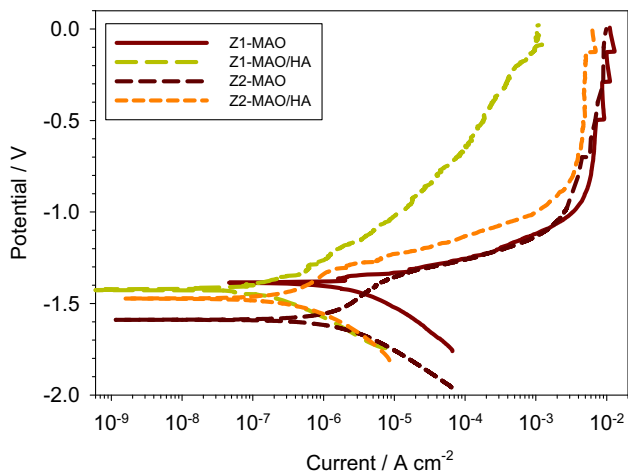


**Fig. 11** Potentiodynamic polarization curves of MAO and MAO-/HA-coated Z1 and Z2 samples in the SBF solution

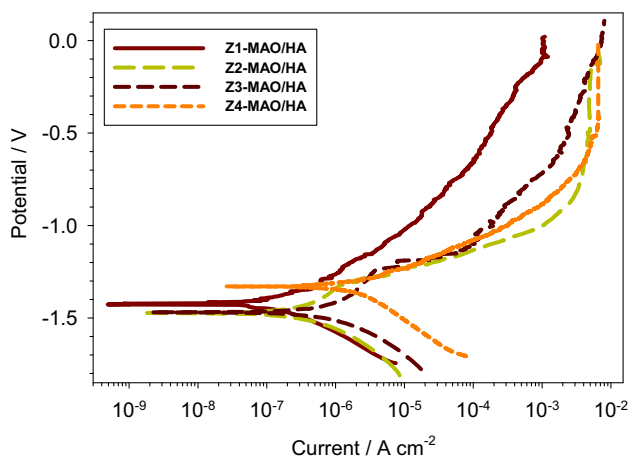


**Fig. 12** Potentiodynamic polarization curves of MAO-/HA-coated Mg-Zn samples in the SBF solution

not properly protected. The deep cracks observed on this specimen could be attributed to strong hydrogen evolution and dehydration of the corrosion products in the corroded layer after drying in warm air.

It is shown that Z2 gave the highest corrosion resistance, which could be related to the grain refinement exerted by the 2 wt.% Zn. At higher Zn wt.% (Z3 and Z4), the precipitated second phase ( $MgZn_2$ ) caused a drop in the corrosion resistance.

**3.3.2 Potentiodynamic Polarization Curves of Uncoated and Coated Mg-Zn Alloys.** Potentiodynamic polarization curves of two MAO-treated samples and four MAO-/HA-coated samples are shown in Fig. 11 and 12, respectively. The HA coating of MAO-treated samples enhances markedly the corrosion resistance of the Mg-Zn alloys as indicated by the shift of anodic current toward more noble values. The best performance of MAO-/HA-coated samples is given by Z1 sample. The highest performance shown by Z1 alloy (one solid solution phase) could be related to better surface homogeneity leading to better adhesion of MAO/HA coating. The presence of zinc may negatively affect the power of the arc formed during MAO process.

The enhancement of corrosion resistance of MAO-/HA-coated magnesium alloys in SBF medium can be illustrated as follows (Ref 33, 34):

After immersion, the SBF electrolyte penetrates through the large pores in the outer porous layer to reach the interface with the inner dense layer. However, the SBF electrolyte does not penetrate through the dense layer to reach the coating/substrate interface at short immersion because of the protective property of the inner dense layer. Pores within the outer porous layer are blocked owing to the volume expansion effect, resulting from the conversion of  $MgO$  to  $Mg(OH)_2$ .

Increasing immersion time results in penetrating both the outer porous layer and the partial inner dense with  $Cl^-$  ions causing the corrosion of alloy substrate.

After long immersion time, a large amount of  $MgO$  is converted to lower density  $Mg(OH)_2$  in the pores. As a result, slow thinning of the  $MgO$  dense layer and volume expansion has occurred and caused further cracking of the micro-arc oxidation film. The cracks provide another pathway for penetration of  $Cl^-$  ions and accelerate the hydration of  $MgO$  within the coating.

## 4. Conclusions

Zn was selected in this work to develop some biodegradable magnesium alloys for biomedical applications due to its good biocompatibility. Microstructure characterizations of Mg-Zn (1-4 wt.%) were investigated. Coating effect was also investigated. Corrosion behavior of the alloys was thoroughly studied. From the results obtained, the following conclusions could be submitted:

1. The microstructure of the as-cast Mg-Zn alloys is composed of  $\alpha$ -Mg and secondary phases, which precipitated along the grain boundaries. In addition, the grain size of Mg decreases with increasing Zn content.
2. The x-ray diffraction pattern showed that the predominant phases of Mg-Zn alloys were  $\alpha$ -Mg and the second phase ( $MgZn_2$ ). SEM micrographs and EDS analysis of Mg-Zn alloys reveal the presence of primary  $\alpha$  dendrites and one or more second phases at the grain boundaries and in the interdendritic regions (Mg,Zn) having strip and rod-like shapes. It was found that up to 2 wt.% Zn, Zn is completely dissolved in the  $\alpha$ -Mg matrix. With increasing Zn content, the second  $MgZn_2$  phase is precipitated.
3. Mg alloys with 1, 2, and 3 wt.% Zn have almost the same corrosion rates (0.025 mm/year); however, the Mg alloy with 4 wt.% Zn obtained higher corrosion rate.
4. Through HA coating on MAO-treated magnesium alloys, a dense and compact layer is formed on the surface of magnesium alloys by which its surface property has largely improved.

## Acknowledgment

This research was financially supported by the Science and Technology Development Fund (STDF), Egypt, Project Grant No. ID: 5342.

## References

1. G.L. Song, Control of Biodegradation of Biocompatible Magnesium Alloys, *Corros. Sci.*, 2007, **49**, p 1696–1701
2. F. Witte, V. Fischer, and J. Nellesen, In Vitro and In Vivo Corrosion Measurements of Magnesium Alloys, *Biomaterials*, 2006, **27**, p 1013–1018
3. M.P. Staiger, A.M. Pietak, J. Huadmai, and G.J. Dias, Magnesium and Its Alloys as Orthopedic Biomaterials: A Review, *Biomaterials*, 2006, **27**, p 1728–1734
4. G.L. Song and S.-Z. Song, Corrosion Behaviour of Pure Magnesium in a Simulated Body Fluid, *Acta Phys. Chim. Sin.*, 2006, **22**(10), p 1222–1226
5. H. Hamid and J. Coltart, Magnesium: An Essential Nutrient for a Good Biomaterial, *McGill J. Med.*, 2007, **10**, p 105–111
6. R.C. Zeng, W. Dietzel, F. Witte, N. Hort, and C. Blawert, Progress and Challenge for Magnesium Alloys as Biomaterials, *Adv. Eng. Mater.*, 2008, **10**, p B3–B14
7. H. Wang, Y. Estrin, H.M. Fu, G.L. Song, and Z. Zuberova, The Effect of Pre-processing and Grain Structure on the Bio-corrosion and Fatigue Resistance of Magnesium Alloy AZ31, *Adv. Eng. Mater.*, 2007, **9**(11), p 967–972
8. S.M. Abd El Hallem, I.M. Ghayad, M. Eiasa, N. Nassif, M.A. Shoeib, and H. Soliman, Effect of Ultrasonic and Mechanical Vibration on the Corrosion Behavior of Mg-3Zn-0.8Ca Biodegradable Alloy, *Int. J. Electrochem. Sci.*, 2014, **9**, p 2005–2015
9. F. Witte, N. Hort, C. Vogt, S. Cohen, K. Kainer, R. Willumeit, and F. Feyerabend, Degradable Biomaterials Based on Magnesium Corrosion, *Curr. Opin. Solid State Mater. Sci.*, 2008, **12**, p 63–72
10. A.D. Südholz, N. Birbillis, C.J. Bettles, and M.A. Gibson, Corrosion Behavior of Mg-Alloy AZ91E with a Typical Alloying Additions, *J. Alloys Compd.*, 2009, **47**, p 109–115
11. C.S. Roberts, *Magnesium and its Alloys*, Wiley Series on the Science and Technology of Materials, Wiley, New York, 1960
12. Y. Wan, G. Xiong, H. Luo, F. He, Y. Huang, and X. Zhou, Preparation and Characterization of a New Biomedical Magnesium-Calcium Alloy, *Mater. Des.*, 2008, **29**, p 2034–2037
13. S. Zhang, X. Zhang, C. Zhao, J. Li, Y. Song, C. Xie, H. Tao, Y. Zhang, Y. He, and Y. Jiang, Research of Mg-Zn alloy as degradable biomaterial, *Acta Biomater.*, 2010, **2**, p 626–640
14. C.S. Dunleavy, I.O. Golosnoy, J.A. Curran, and T.W. Clyne, Characterisation of Discharge Events During Plasma Electrolytic Oxidation, *Surf. Coat. Technol.*, 2009, **203**(22), p 3410–3419
15. J. Curran and T. Clyne, Thermo-Physical Properties of Plasma Electrolytic Oxide Coatings on Aluminium, *Surf. Coat. Technol.*, 2005, **199**(2-3), p 168–176
16. J.H. Gao, S.K. Guan, J. Chen, L.G. Wang, S.J. Zhu, J.H. Hu, and Z.W. Ren, Fabrication and Characterization of Rod-Like Nano-hydroxyapatite on MAO Coating Supported on Mg-Zn-Ca Alloy, *App. Surf. Sci.*, 2011, **257**, p 2231–2237
17. G.Y. Liu, J. Hu, Z.K. Ding, and C. Wang, Formation Mechanism of Calcium Phosphate Coating on Micro-arc Oxidized Magnesium, *Mater. Chem. Phys.*, 2011, **130**, p 1118–1124
18. N.N. Girgis and I.M. Ghayad, Corrosion Protection and Surface Treatment of Magnesium Alloys Used for Orthopedic Application, *Adv. Mater. Sci. Eng.*, 2013, doi:10.1155/2013/532896
19. Z. Qiao, Z. Shi, N. Hort, N.I. Zainal Abidin, and A. Atrens, Corrosion Behavior of a Nominally High Purity Mg Ingot Produced by Permanent Mould Direct Chill Casting, *Corros. Sci.*, 2012, **61**, p 185–207
20. Z. Shi and A. Atrens, An Innovative Specimen Configuration for the Study of Mg Corrosion, *Corros. Sci.*, 2011, **53**, p 226–246
21. Y. Lu, “Microstructure and Degradation Behaviour of Mg-Zn(-Ca) Alloys,” Ph.D. thesis, School of Metallurgy and Materials, University of Birmingham, UK, 2014
22. A. Nayeab-Hashemi and J.B. Clark, *Phase Diagrams of Binary Magnesium Alloys*, ASM, Metals Park, 1988
23. M.A. Easton and D.H. St John, A Model of Grain Refinement Incorporating Alloy Constitution and Potency of Heterogeneous Nucleant Particles, *Acta Mater.*, 2001, **49**, p 1867–1878
24. D.H. St John, M. Qian, M.A. Easton, P. Cao, and Z. Hildebrand, Grain Refinement of Magnesium Alloys, *Metall. Mater. Trans. A Phys. Metall. Mater. Sci.*, 2005, **36**(7), p 1669–1679
25. Y. Lu, A.R. Bradshaw, Y.L. Chiu, and I.P. Jones, Effects of Secondary Phase and Grain Size on the Corrosion of Biodegradable Mg-Zn-Ca Alloys, *Mater. Sci. Eng. C*, 2015, **48**, p 480–486
26. Q. Li, J. Liang, and Q. Wang, Plasma Electrolytic Oxidation Coatings on Light Weight Metals, *Modern Surface Engineering Treatments*, M. Aliofkhaizraei Ed., ISBN 978-953-51-1149-8, 2013
27. J.Z. Li, Z.C. Shao, Y.W. Tian, F.D. Kang, and Y.C. Zhai, Application of Microarc Oxidation for AlMg, Ti and Their Alloys, *Corros. Sci. Protect. Technol.*, 2004, **6**(4), p 218–221
28. J.A. Curran and T.W. Clyne, Porosity in Plasma Electrolytic Oxide Coatings, *Acta Mater.*, 2006, **54**, p 1985–1993
29. Z.G. Huan, M.A. Leeftang, J. Zhou, L.E. Fratile-Apachitei, and K.J. Duszczyn, In Vitro Degradation Behavior and Cytocompatibility of Mg-Zn-Zr Alloys, *J. Mater. Sci. Mater. Med.*, 2010, **21**, p 2623–2635
30. G. Song, A. Atrens, X. Vu, and B. Zhang, Corrosion Behavior of AZ21, AZ501 and AZ91 in Sodium Chloride, *Corros. Sci.*, 1998, **40**(10), p 1769–1791
31. C.L. Wen, S.K. Guan, L. Peng, C.X. Ren, X. Wang, and Z.H. Hu, Characterization and Degradation Behavior of AZ31 Alloy Surface Modified by Bone-Like Hydroxyapatite for Implant Applications, *Appl. Surf. Sci.*, 2009, **255**, p 6433–6438
32. S.J. Xia, R. Yue, J.R.G. Rateick, and V.I. Birss, Electro/Chemical Studies of AC/DC Anodized Mg Alloy in NaCl Solution, *J. Electrochem. Soc.*, 2004, **151**, p B179–B187
33. W. Suhanec and M. Yoshimura, Processing and Properties of Hydroxyapatite-Based Biomaterials for Use as Hard Tissue Replacement Implant, *J. Mater. Res.*, 1998, **13**, p 94–117
34. L. Liu, P. Yang, C. Su, H. Guo, and M. An, Microstructure and Corrosion Behavior of Micro-arc Oxidation Film on Magnesium Alloy, *Int. J. Electrochem. Sci.*, 2013, **8**, p 6077–6084